Infrared Physics & Technology 150 (2025) 105988

Contents lists available at ScienceDirect

Infrared Physics and Technology

journal homepage: www.elsevier.com/locate/infrared

Cascaded Fabry-Perot interferometric air bubble strain sensor for finger motions

Yanshu Zeng [a], Xianli Li [a,*], Jingwei Lv [a], Jianxin Wang [a], Hongze Zou [b], Wei Liu [a], Chao Liu [a,*], Paul K Chu [c]

[a] School of Physics and Electronic Engineering, Northeast Petroleum University, Daqing 163318, PR China
[b] The Second Oil Production Plant of Daqing Oilfield Co. Ltd., Daqing 163318, PR China
[c] Department of Physics, Department of Materials Science and Engineering, and Department of Biomedical Engineering, City University of Hong Kong, Tat Chee Avenue, Kowloon, Hong Kong, China

ARTICLE INFO

Keywords:
Strain sensor
Fabry-Pérot Interference
Micro air bubbles
Finger motion detection

ABSTRACT

Strain sensors have important applications in health monitoring. Herein, a cascaded air bubble strain sensor based on Fabry-Perot interference is designed and analyzed. By using single-mode optical fibers, cascaded air bubbles are fabricated as the sensing elements. The external environment alters the wall thickness of the air bubbles and, consequently, the interference spectra. The sensor can detect strains in the range of 0–1200 με with a sensitivity of 11.07 pm/με. Considering the temperature cross-sensitivity, the sensor is placed in a thermostatic heating platform and heated to 100 °C. The temperature cross-sensitivity is 0.2 με/°C. To demonstrate the practicality, the sensor is fixed on fingers to sense the bending motion of joints. Experimental results confirm high strain sensitivity and low temperature cross-sensitivity. As the sensor also offers good repeatability and stability for strain sensing, it has immense potential in applications such as finger rehabilitation training and gesture recognition.

1. Introduction

Strain sensors have been extensively used in human health monitoring. For example, they can be attached to muscles and finger joints to sense finger flexion, gesture, and motion [1–3]. Compared with other types of strain sensors, fiber strain sensors have high accuracy, strong resistance to electromagnetic interference, and the ability to make distributed measurements. A variety of fiber strain sensors based on different structures have been proposed, for instance, fiber Bragg grating (FBG) strain sensors [4], interferometric strain sensors (Mach-Zehnder interferometer (MZI) [5], Sagnac interferometer [6,7], and Fabry-Perot interferometer (FPI) [8,9,10]. Strain is monitored by detecting the phase, intensity, and wavelength changes of the sensors. FBG sensors are stable and have a simple structure. Under strain, the grating periodicity in the fiber core and refractive index (RI) change to produce shifts in the interference spectrum. However, FBG strain sensors are sensitive to temperature changes in the environment, and the cross-sensitivity leads to inaccuracy requiring temperature compensation [11]. In contrast, interferometer sensors do not require sophisticated demodulation equipment, and the temperature cross-sensitivity can be reduced by altering the structure and changing the filler materials [12]. Hence, FPI strain sensors have many advantages such as high sensitivity, simple structure, and temperature insensitivity. Particularly in the field of wearable health monitoring, FPI fiber optic sensors are used for monitoring respiration as well as joint activity. MARIA et al. [13] embedded fiber optic FPI sensors in a Kinesio tape (K-tape) and placed them in polylactic acid (PLA) and epoxy resin for ankle kinematics monitoring. Shi et al. [14] combined a single-mode optical fiber with a capillary tube and coated the end of the latter with an agar film to create an FPI structure. The moisture absorption of the agar film in a high relative humidity environment was utilized to monitor the respiratory humidity.

FPI is a multi-beam interference phenomenon occurring between two parallel reflecting surfaces which form an interference cavity. The cavity length of the interference cavity affects the periodic characteristics of the interference spectrum. Therefore, the performance of the sensor can be significantly improved by optimizing the structural parameters of the interference cavity. Composite FPI sensors have been studied. Lin et al. [10] have fused a suspended-core fiber (SCF) with a

* Corresponding authors.
E-mail addresses: lxl7158@163.com (X. Li), msm-liu@126.com (C. Liu).

https://doi.org/10.1016/j.infrared.2025.105988
Received 25 March 2025; Received in revised form 16 June 2025; Accepted 20 June 2025
Available online 21 June 2025

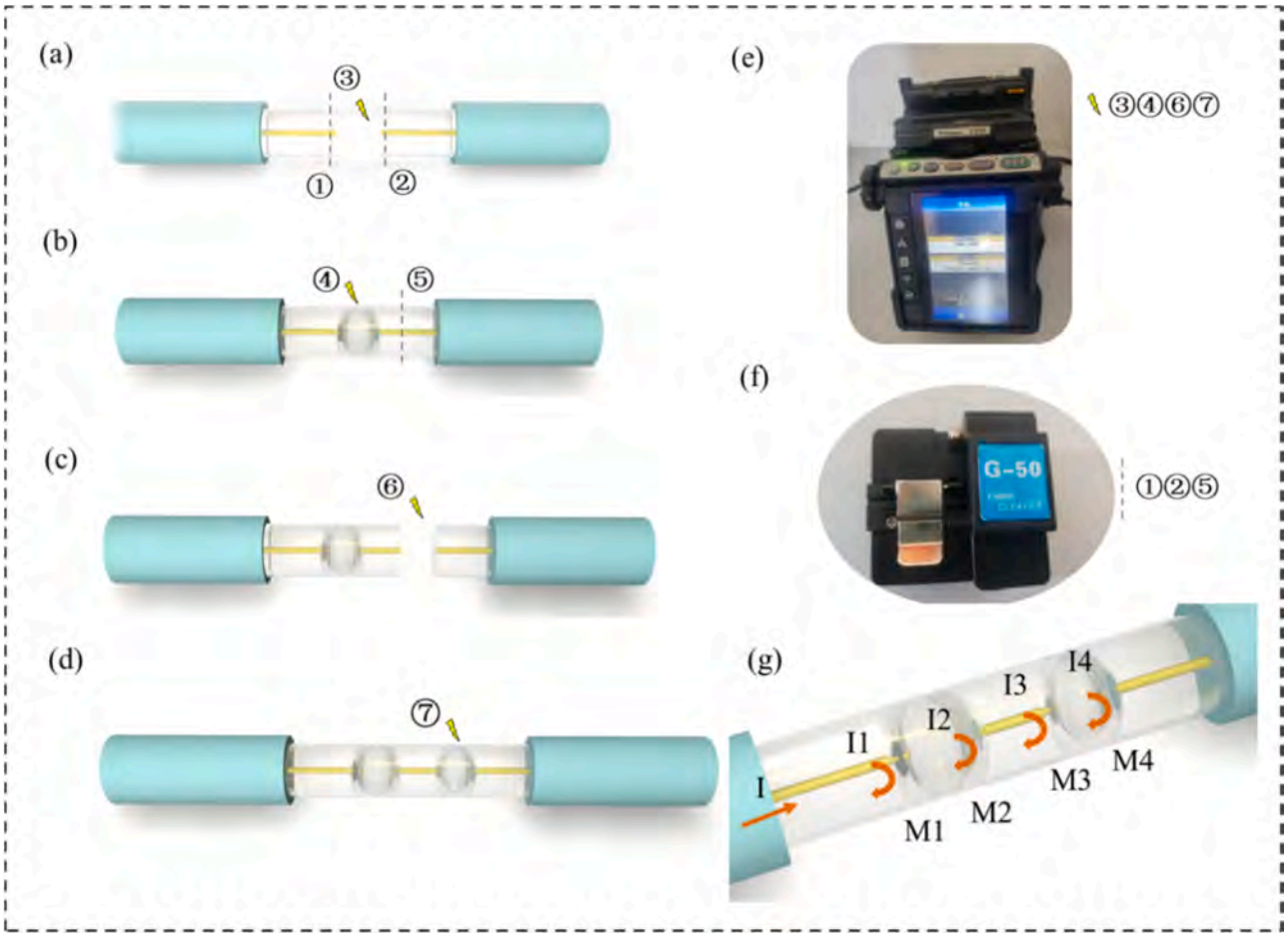

Fig. 1. Preparation of the cascaded air bubbles strain sensor.

single-mode fiber (SMF) and partially collapsed the SCF through a discharge to form the FPI cavity. The sensor can algorithmically extract temperature and strain independently enabling two-parameter measurements. Zhang et al. [15] have proposed a temperature and motion sensor based on the Vernier effect and FPI. In the sensor, an eccentric core fiber (ECF) and a double-side hole fiber (DSHF) are fused to generate two FPI cavities. Wang et al. [16] have studied a fiber strain sensor based on cascaded MZI and FPI. The sensor adopts the SMF-no core fiber (NCF)-hollow core fiber (HCF)-NCF-SMF structure to produce the MZI cavity and uses HCF as the FPI cavity.

Composite sensors can accomplish multi-parameter measurements, and the cascade of interferometric cavities can achieve sensitization by means of the superposition of spectra, leading to the Vernier effect. However, the cascading methods of some complex structures have high requirements for process precision during the fabrication process, increasing the difficulty of implementation. In this respect, the bubble-based FPI sensors have attracted attention. In the sensor, bubbles are formed inside the optical fiber by chemical etching or fusion bonding, and the thin walls of the bubbles can be regarded as two parallel reflective surfaces forming an interference cavity. Common types of bubble interference cavities are circular bubbles [17], round rectangular bubbles [18], and elliptical bubbles [19]. To improve the strain sensitivity, structures comprising eccentric-core fibers [17], asymmetrical fibers [20], and tapered fibers [21] have been proposed for these different types of air bubbles. These air microbubbles have a low production cost and the manufacturing can be done by fiber optic fusion splicing. In the field of using bubble interference structures to measure axial strain, Wang et al. [22] proposed a micro-bubble FPI based on tapered hollow-core fiber. They utilized the arc discharge tapering technique to prepare micro-bubbles inside the HCF. Lu et al. [23] achieved sensitivity enhancement by taking advantage of the Vernier effect of the cascaded dual-bubble FPI. They used femtosecond lasers to inscribe two short lines inside a single-mode fiber and then formed two adjacent bubble cavities through a splicing operation. Tian et al. [24] embedded a tapered single-mode fiber probe into the bubble and took the end face of the fiber as the reflecting surface to construct an FPI with an extremely short cavity length. Reducing the wall thickness or adopting a tapered structure can help improve the strain sensitivity, but it will increase the manufacturing difficulty and reduce the structural strength meanwhile.

In this paper, an FPI strain sensor with cascaded air cavity bubbles is presented. The first FPI cavity is fabricated between two SMFs by arc discharge. Near the first FPI cavity, the optical fiber is cut with a precision cutter, and the optical fiber with the FPI cavity is fused with another SMF to create the second FPI cavity. The experimental results show that the strain sensor has a sensitivity of 11.07 pm/με and can measure strain in the range of 0–1200 με. Furthermore, the sensor has a temperature sensitivity of 2.2 pm/°C and cross-sensitivity of 0.20 με/°C in the temperature range of 22 °C-100 °C, indicating that the sensor is not sensitive to temperature. The sensor is innovatively fixed to the finger joint and successfully captures the characteristic spectra corresponding to the three bending degrees. The feasibility of the cascaded double air cavity structure in the finger motion monitoring is verified for the first time. Its excellent stability and repeatability have provided a low-cost and reliable solution for wearable strain monitoring in the field of medical rehabilitation.

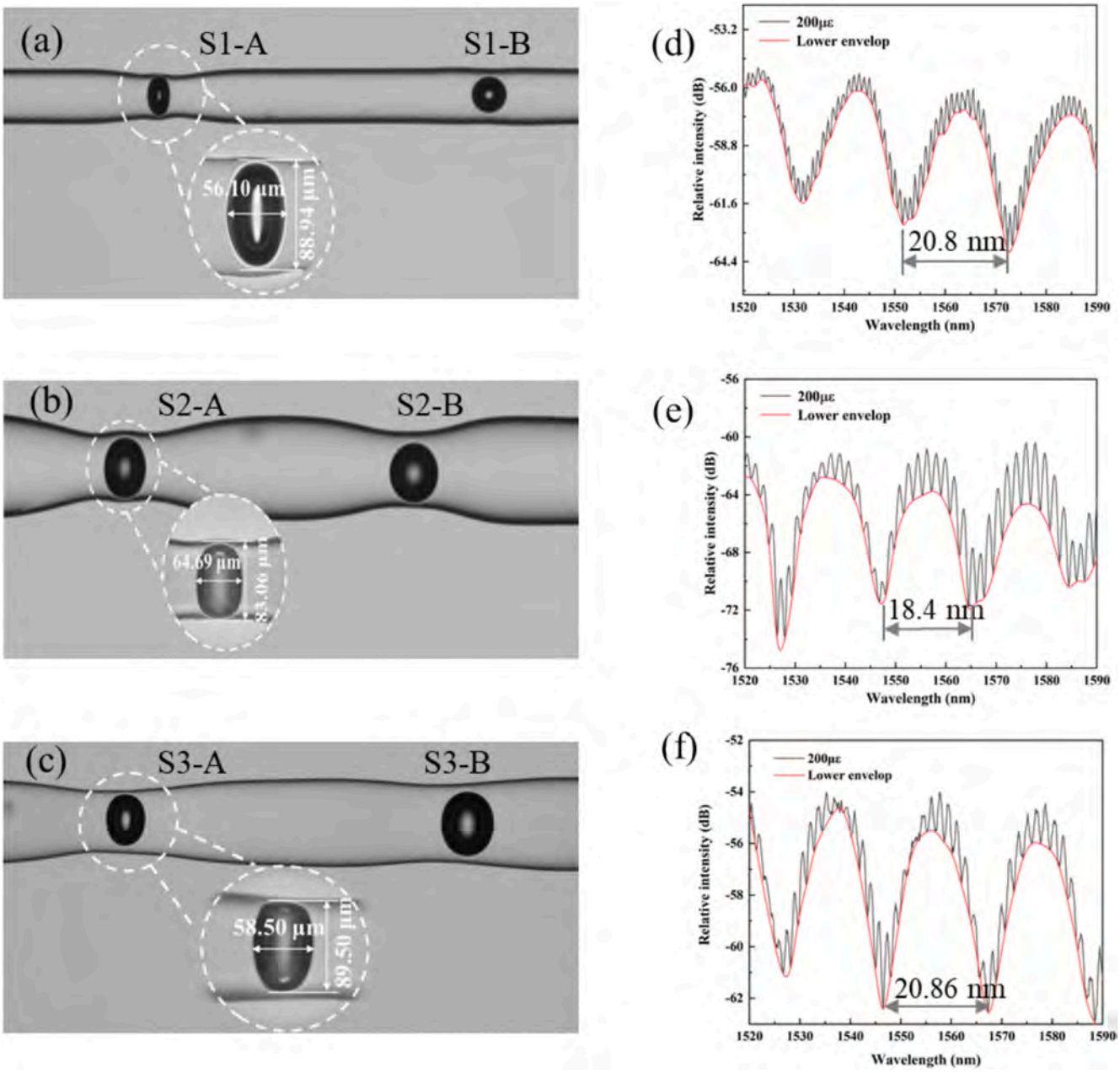

Fig. 2. Microscopic image and spectrum of the three sensors.

Table 1
Dimensions of the three sensors.

Name	Axial length-A (μm)	SiO_2 Length (μm)	Axial length-B (μm)	Upper bubble wall thickness-A (μm)	Bottom bubble wall thickness-A (μm)
S1	56.10	663.1	91.08	3.46	6.6
S2	64.69	529.58	89.8	6.5	4.5
S3	58.50	434.7	78.3	4.2	6.7
mean	59.76333	542.46	86.39333	4.72	5.93333
Standard deviation	4.43216	114.74346	7.03819	1.58531	1.24231

2. Fabrication process, principle, and experimental setup

Precise bubble regulation can be achieved by adjusting the parameters of the optical fiber fusion splicer. Currently, many efforts have been devoted to bubble fabrication techniques using fiber fusion splicers, achieving high-precision control of bubble dimensions, positioning, and morphology [25,26]. Fig. 1 shows the preparation process of the cascaded bubbles-based strain sensor. The coating on the single-mode fiber was removed, and the fiber port was cut by a fiber cutter, as shown in Fig. 1(f). The sample was put into a fiber fusion splicer (Fujikura 80 s, shown in Fig. 1(e)), and the discharge power was set so that the fiber ports had a smooth arc shape, as shown in Fig. 1(a).

$$I = I_1 + I_2 + I_3 + I_4 + 2\sqrt{I_1 I_2}\cos(\Delta\Phi_1) + 2\sqrt{I_1 I_3}\cos(\Delta\Phi_2) + 2\sqrt{I_1 I_4}\cos(\Delta\Phi_1 + \Delta\Phi_2) + 2\sqrt{I_2 I_3}\cos(\Delta\Phi_2 - \Delta\Phi_1) + 2\sqrt{I_2 I_4}\cos(\Delta\Phi_2) + 2\sqrt{I_3 I_4}\cos(\Delta\Phi_1) \quad (1)$$

Subsequently, the fiber end face was dipped in a small amount of RI matching fluid (Nd:1.47). The RI matching liquid was similar to the RI of the optical fiber, thus reducing reflections from the fiber end face. The round end face reduced light scattering at the fiber end face and also increased the contact area with the RI-matching liquid. Under the effect of liquid surface tension, the gas was wrapped inside the liquid film, which was conducive to the formation of stable bubbles. The air inside the bubble had a different RI than the optical fiber and constituted the interference cavity of the FPI. The optical fiber was dipped in the RI matching liquid and placed in the optical fiber fusion splicer. The fusion splicing mode was set to "SMF-SMF" and the discharge power and time were set to "+20″ and "1,200 ms", respectively. After tiny bubbles were formed inside the optical fiber, the position of the fusion splicer motor and the discharge time and power were adjusted to change the size and shape of the bubbles. When the two motors moved outward to apply tensile stress to the optical fiber, the shape of the bubble tended to be round. If the motors moved inward to apply extrusion stress to the optical fiber, the shape of the bubble tended to be elliptical. As the bubble expanded, the discharge power and time were reduced to make fine adjustments to the size of the bubble and decrease the wall thickness between the bubble and the fiber cladding. After the first air cavity was prepared, a knife was used to cut the fiber beside the bubble. The operations are shown in Fig. 1(b). Another single-mode fiber with an FPI cavity was placed in the fiber fusion splicer, and step (a) was repeated, as shown in Fig. 1 (c). Subsequently, step (b) was repeated to form a second air cavity by multiple discharges at the fusion splice, as shown in Fig. 1 (d), in which steps ③, ④, ⑥, and ⑦ indicate arc discharge, while steps ①, ②, and ⑤ indicate flattening of the end face with a fiber optic cutter. All in all, the FPI can be prepared by only a fiber optic fusion splicer, and the preparation process is simple, economical, and practical.

Fig. 1(g) shows the schematic diagram of the FPI sensor. The sensor consists of four reflective surfaces, M1, M2, M3, and M4 formed by two air cavities. Light from a light source undergoes multiple transmissions and refractions at the bubble interface to produce four beams of interfering light, I1, I2, I3, and I4. The total light intensity of the interfering light can be expressed as [19]:

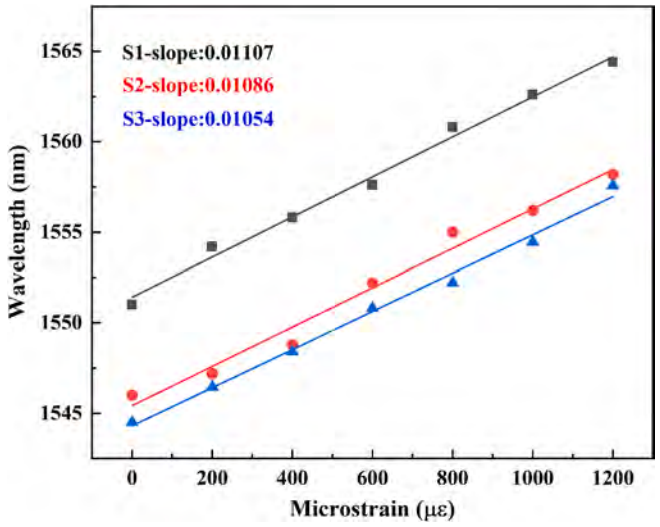

Fig. 3. Strain sensing fitting curves for the three sensors.

where $I_i|E_i|^2$ is the beam intensity and $\Delta\Phi_2$ are the phase differences between the light propagating in the two FPI cavities:

$$\begin{cases} \Delta\Phi_1 = \dfrac{4\pi n_1 L_1}{\lambda} \\ \Delta\Phi_2 = \dfrac{4\pi n_2 L_2}{\lambda} \end{cases} \quad (2)$$

where, $\boldsymbol{n_1}$ and $\boldsymbol{n_2}$ are the effective RIs of the two FPI cavities, $\boldsymbol{L_1}$ and $\boldsymbol{L_2}$ are the cavity lengths of the two FPI cavities, and $\boldsymbol{\lambda}$ is the wavelength of the incident light. Equation (1) shows that the interference spectrum is a linear superposition of multiple cosine signals, and its distribution depends on the light intensity and phase difference of each beam.

The free spectral range (FSR) [27], an important parameter of FPI, reflects the bandwidth of the interferometer for processing optical signals. FSR is the wavelength separation between two interference peaks in the interference spectrum. The phase difference between two neighboring interference peaks is expressed as:

$$\frac{4\pi nL}{\lambda_m} - \frac{4\pi nL}{\lambda_{m+1}} = 2\pi \quad (3)$$

where $\boldsymbol{\lambda_m}$ and $\boldsymbol{\lambda_{m+1}}$ denote the wavelengths corresponding to the two neighboring peaks, and L is the length of the bubble cavity. Approximately, $\lambda_m \approx \lambda_{m+1} = \lambda$. The FSR can be expressed as:

$$\Delta L = \frac{\lambda^2}{2nL} \quad (4)$$

By applying axial strain to the fiber, the cavity length changes thereby affecting the interference of the transmitted light. This is manifested as changes in both the interference light intensity and the position of the interference peaks. The microstrain imposed on the fiber optic sensor can be expressed as [20]:

$$\varepsilon = \frac{\Delta L}{L} \quad (5)$$

where $\Delta\boldsymbol{L}$ represents the change in the cavity length under strain. The microstrain sensitivity can be expressed as the change in the wavelength corresponding to the interference light peak caused by unit strain, and its expression is shown in the following:

$$S_\lambda = \frac{\Delta\lambda}{\varepsilon} \quad (6)$$

By monitoring the variation of the wavelength corresponding to the interference peak, the magnitude of the externally applied strain can be inversely deduced. Higher micro-strain sensitivity leads to a more pronounced change in the corresponding wavelength, indicating that the sensor is capable of detecting minute strain variations with great sensitivity.

Three sensors (S1, S2, and S3) were fabricated by means of the method mentioned above. Their microscopic images and corresponding optical spectra are presented in Fig. 2. The key parameters including axial bubble length, inter-bubble distance, and bubble wall thickness are summarized in Table 1. Fig. 2(a) depicts the 4x microscopic image of the sensor. The interval between the two air cavities of the sensor is 663.1 μm. The cavity lengths of the first air bubble S1-A are 88.94 μm and 56.10 μm, while those of the second air bubble S1-B are 84.18 μm and 91.08 μm. By adjusting the discharge time and power of the fiber fusion splicer, the wall thickness between the fiber and the air bubbles can be reduced. When slight changes occur in the external environment, a

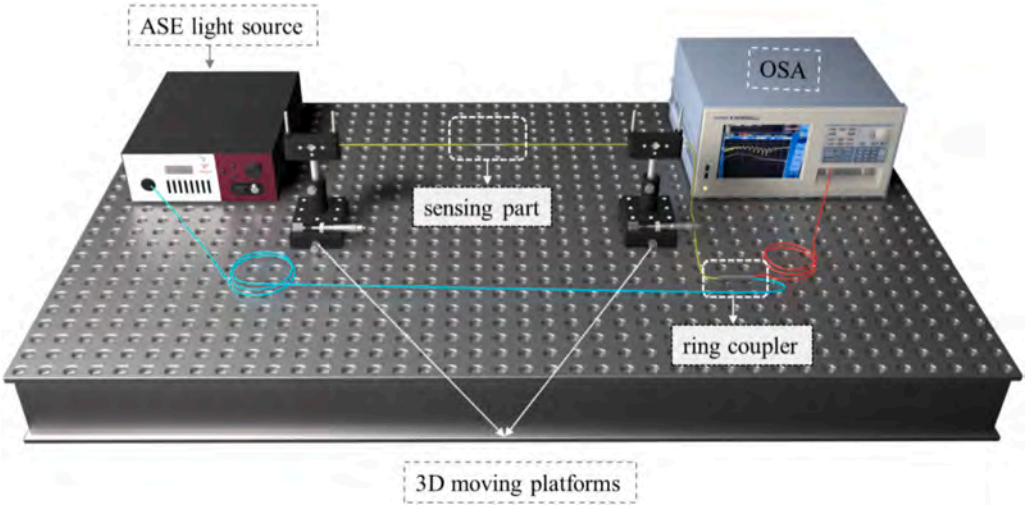

Fig. 4. Experimental platform for the strain measurement.

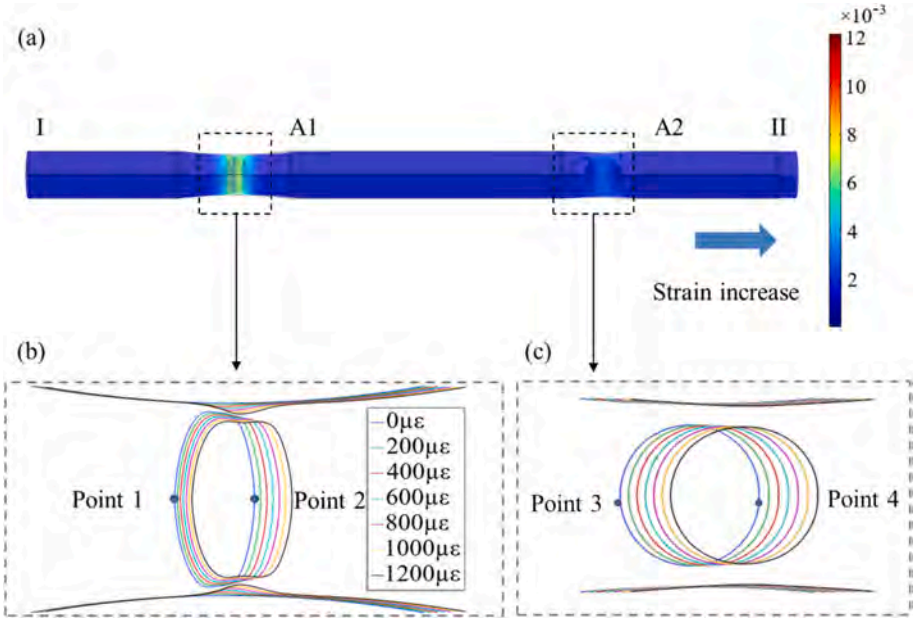

Fig. 5. Simulated results: (a) Strain response of the sensor; Deformation of (b) Bubble A1 and (c) Bubble A2 under different stresses.

smaller wall thickness enables stress to act on the bubbles, making the bubbles more prone to deformation. The alteration of the cavity length causes the interference spectrum to shift, and by analyzing the changes in the interference peaks, the micro-stress can be measured. According to Equation (1), the spectrum is a superposition of multiple cosine signals, and therefore, the interferometric light intensity has a zigzag shape. The data listed in Table 1 demonstrate that this strain sensor preparation process exhibits excellent repeatability. FSRs of the three sensors are 20.8 nm, 18.4 nm, and 20.86 nm, respectively. Fig. 3 presents the strain-wavelength fitting curves for the three sensors, indicating that all three curves exhibit similar linearity. Moreover, These results confirm that variations in bubble size and relative positioning have negligible impact on sensing sensitivity, whereas sensitivity shows strong dependence on bubble wall thickness.

Fig. 4 illustrates the experimental setup for the strain measurement. In the sensing experiment, the distance between the three-dimensional moving platforms was 40 cm, and both ends of the sensor were fixed on the three-dimensional moving platforms. One end of the sensor was connected to an amplified spontaneous emission light source (ASE, 450——2500 nm) and optical spectrum analyzer (OSA, resolution 0.02 nm) separately through a ring coupler. Light emitted from the ASE light source was transmitted to the sensor through the ring coupler, and the reflected light signal was then transmitted back to the OSA through the coupler to obtain the interference spectrum. The movement of the three-dimensional platform exerted axial strain on the sensor, and for every 10 μm increase in platform movement, a strain of 25 με is applied to the sensor.

3. Results and discussion

Fig. 5 shows the strain response of the sensor simulated by COMSOL finite element analysis [28,29]. To observe obvious deformation, the scale factor is set to 20. One end (End I) of the sensor is fixed, and a strain of 1200 με is applied to the other end (End II). The simulation results of the stress distribution are shown in Fig. 5(a). The color gradient represents the distribution of the axial stress on the sensor. It is seen that the A1 air cavity, with its thinner wall thickness, experiences significantly higher axial stress than cavity A2, confirming that thinner bubble walls yield higher strain sensitivity. Fig. 5(b) illustrates the deformation characteristics under 0–1200 με strain. Compared with single-bubble

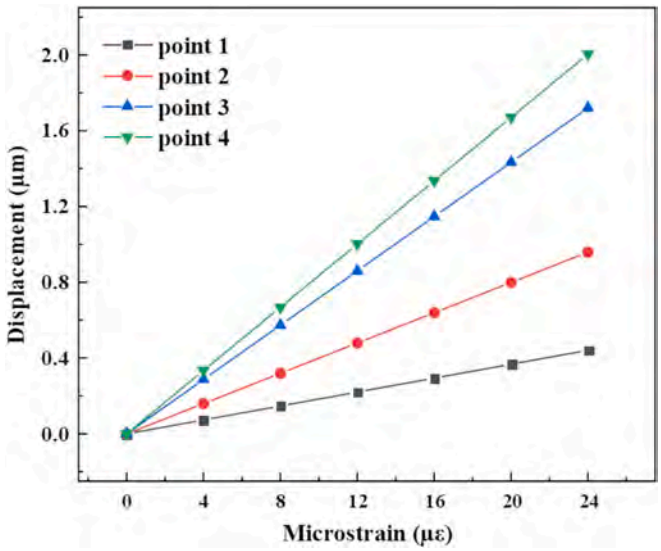

Fig. 6. Variation of microbubble parameters.

sensors prone to irreversible damage caused by stress concentration, the cascaded structure enhances stability by distributing stress. Fig. 6 shows the displacement changes of four points on the sensor air cavity under different strains. Simulations show that the thin-walled A1 has small displacement and large deformation, high sensitivity, and rapid response, while the thick-walled A2 has larger displacement and smaller deformation, with anti-overload capability.

The fast Fourier transform (FFT) is used to analyze the main components of the synthetic spectrum. It is seen from Fig. 7(a) that the first-order spatial frequency of sensor S1 is 0.0499 nm^{-1}, corresponding to the air-FP. Due to the existence of the hybrid cavity composed of silicon and air, the second-order spatial frequency is excited. Based on FFT theory, the spatial frequency is the inverse of the FSR [20]. Taking sensor S1 as an example for verification, the FSR of the air FP is approximately 20.8 nm, and its corresponding first-order spatial frequency is about 0.0499 nm^{-1}. Through calculation, the product of the two is approximately equal to 1. The signals generated by different FP cavities are extracted using a bandpass filtering method, as shown in Fig. 7(b). Near the wavelength of 1550 nm, three troughs are observed, labeled V1, V2, and V3. Through measurement, the FSR near the valleys is approximately 20.8 nm and 1 nm. Combining the cavity length of sensor S1 in Table 1 and the relationship between the cavity length and the free spectral range (FSR) expressed by formula (4), it can be judged that the FP cavities corresponding to the extracted curves are accurate. Therefore, this sensor consists of air-FP and silicon-air-FP. Its reflection spectrum exhibits the superposition of multiple cosine signals from multi-beam interference.The original interference spectrum exhibits a zigzag waveform due to multi-beam interference, making direct peak-shift analysis susceptible to noise. To facilitate rapid analysis of the movement of signal peaks, the lower envelope of the curve is plotted. The lower envelope tracks the local minimum of the spectral curve. Extracting the lower envelope provides a clearer representation of the overall drift trend of interference peaks, facilitating the investigation of the strain-wavelength relationship.

The spectra and fitted curves after applying positive and negative strains at room temperature are shown in Fig. 8. During the forward strain application stage, the strain increases from 0 to 1200 με, and the spectral changes are recorded every 200 με. The interference spectrum near a wavelength of 1,550 nm is selected for the analysis. As the strain increases, the interference peak redshifts. The total wavelength shift is 13.4 nm, and the sensitivity of the sensor is 11.07 pm/με. In the reverse strain release stage, the axial strain decreases from 1,200 to 0 με, and the interference peak blueshifts. According to the linearly fitted curves of strain and the corresponding wavelength of the interference peak, the strain sensitivity is 10.96 pm/με. The R-square values of the fitted curves from the two sets of experiments are 0.99211 and 0.98029, respectively. This slight difference may be attributed to the inelasticity of the fiber and the inability of the bubbles to return to their original state shortly

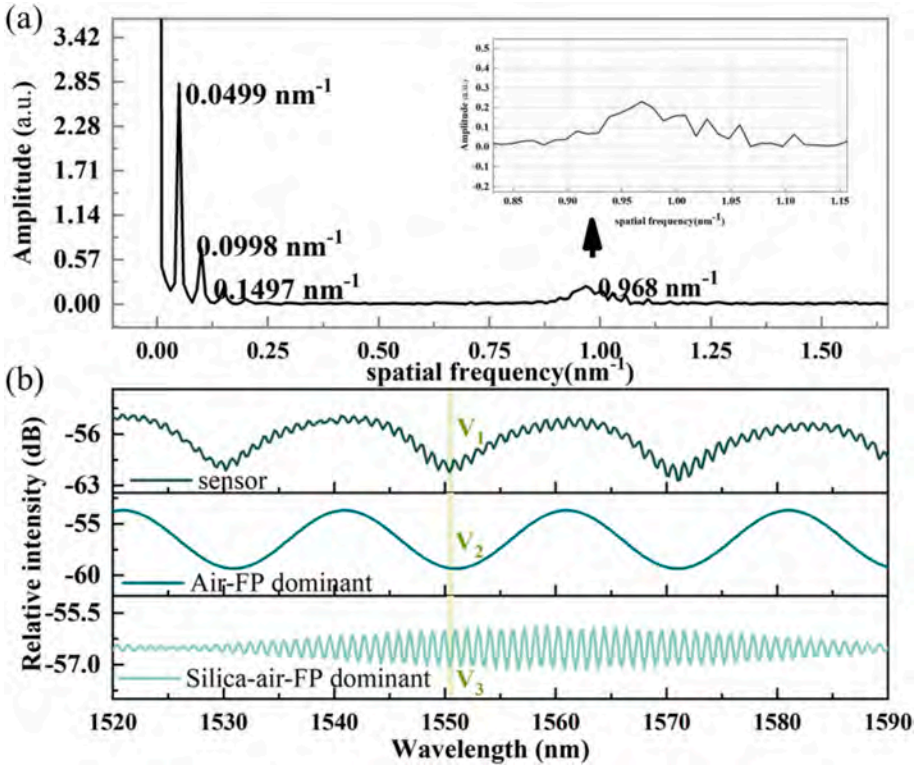

Fig. 7. (a) FFT analysis and (b) Band pass filtering of sensor S1.

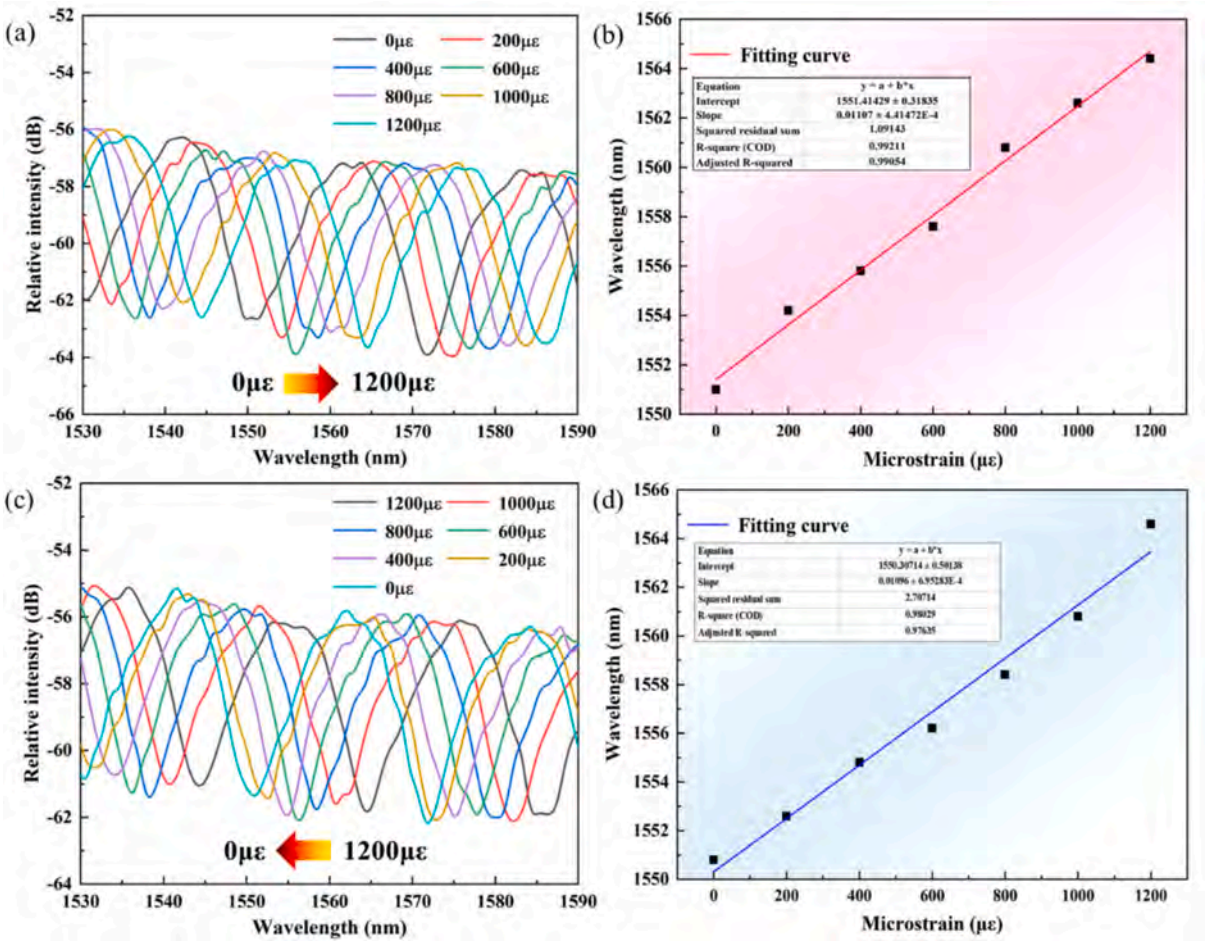

Fig. 8. Stability of the sensor S1 under different strain conditions: (a) Strain applied in the forward direction, (b) Stress released in the reverse direction; (c) and (d) Linearly fitted curves of microstrain versus the corresponding wavelength of the interference peaks for the two sets of experiments.

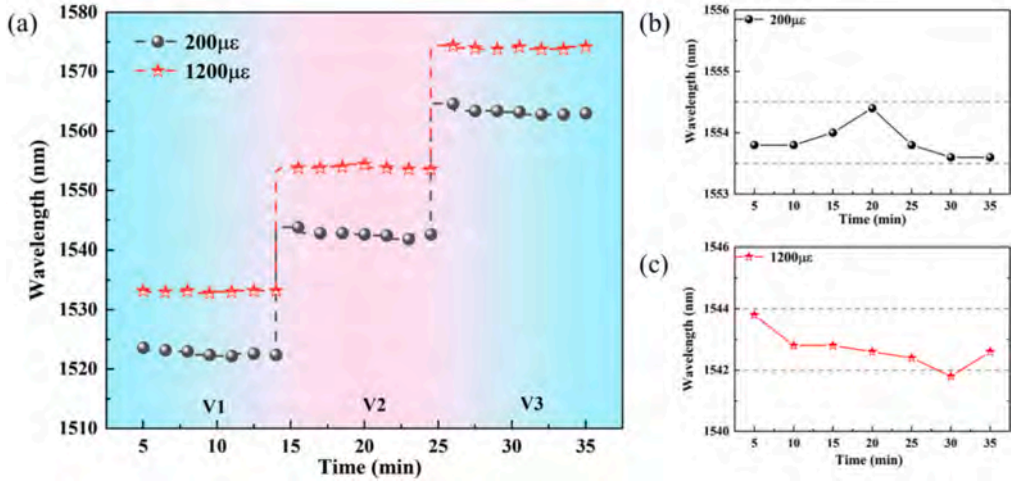

Fig. 9. (a) Stability assessment of the sensor S1; (b) and (c) Magnified views of the wavelength drift of V2.

after deformation. According to Equation (2), the phase difference of light is related to the cavity length of the bubble. The deformation of the bubble changes the cavity length, thereby influencing the position of the interference peaks. By comparing the sensitivity and R-square values of the two stages, the repeatability of the sensor can be verified. Moreover, the FSR affects the measurable strain range. After the strain reaches 1,400 με, the interference peaks overlap, which is unfavorable for observing the changes in the interference peaks. Therefore, the strain range studied is between 0 and 1,200 με.

Fig. 9 shows the stability of the sensor. Under axial strains of 200 με and 1,200 με, the drift of the wavelengths of the three interference peaks (V1, V2, and V3) in the interference spectrum is monitored within 35 min, and data are acquired every 5 min. It can be seen from the experimental results that the wavelengths of the three interference peaks are

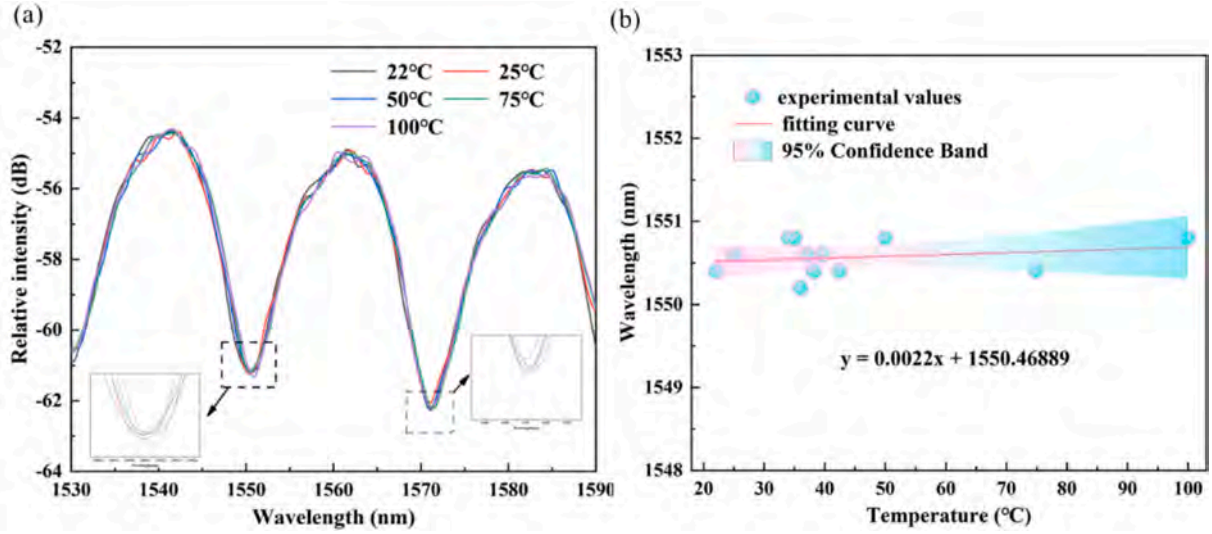

Fig. 10. (a) Temperature response of the sensor S1; (b) Fitted curve for the variation in the corresponding wavelengths of the interference peaks with temperature.

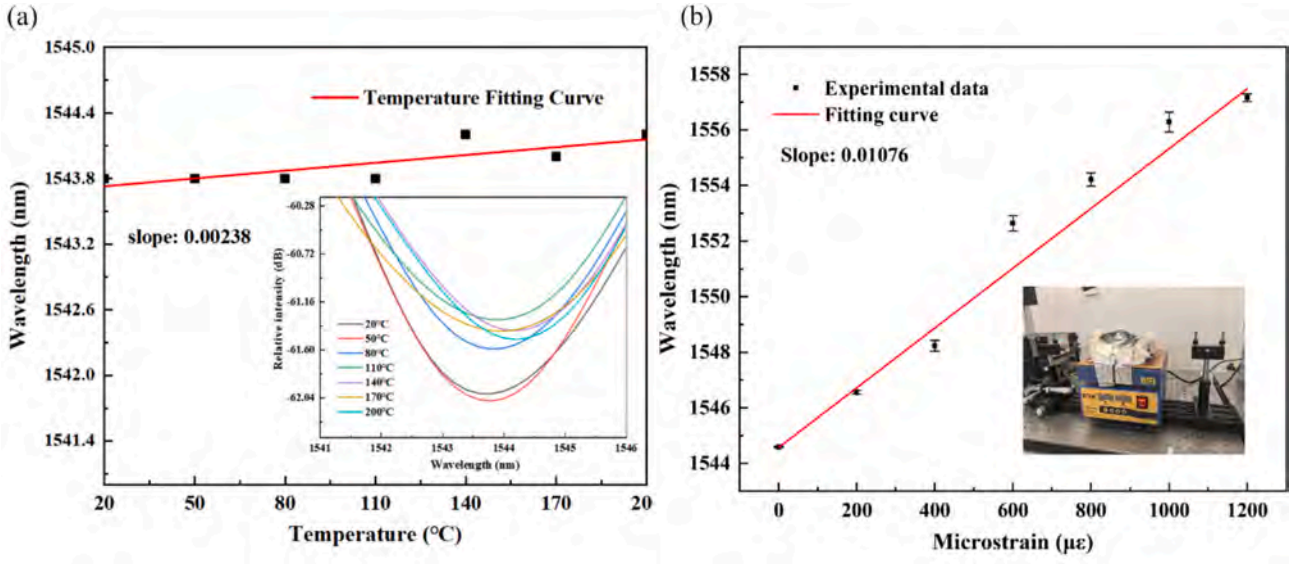

Fig. 11. Sensor S1′s temperature performance in (a) industrial and (b) real environments.

basically consistent within 35 min under the two sets of strains. Fig. 9(b) and 9 (c) show the magnified views to exhibit the degree of wavelength drift of V2. When a constant strain of 200 με is applied, the wavelength change is less than 0.8 nm. Obvious fluctuations in the wavelength occur at 20 min, while the changes are relatively small at other times. Such fluctuations may be caused by interferences from the external environment, such as slight vibrations of the three-dimensional displacement platform. When a constant strain of 1,200 με is applied, the wavelength change is less than 2 pm. A significant blueshift in the wavelength appears after 5 min and remains basically stable afterward. Obvious fluctuations are observed at 30 min perhaps due to the inelasticity of the fiber or the slow rebound of the wavelength due to the loose clamping of the optical fiber. In the interference spectrum, the wavelength drifts more noticeably under greater strain. This is due to the significant change in the bubble cavity length caused by a larger strain, which then affects the optical path. According to the interference principle, the change in the optical path difference makes the wavelength drift more remarkably. Furthermore, under the action of a large strain for an extended period, the stress distribution inside the bubble becomes uneven (Fig. 5(a)), making light propagation in the interference cavity unstable and causing significant wavelength fluctuations.

Fig. 10 shows the temperature response of the sensor between 22 °C and 100 °C. The increase in temperature has an effect on the thermo-optical effect of the optical fiber and also causes the bubble to expand, resulting in the drift of the interference peak. To evaluate the effect of temperature on the sensor, both ends of the sensor are fixed on a metal base with high-temperature tape and then placed into a thermostatic heating platform. The interference spectra acquired at 22 °C, 25 °C, 50 °C, 75 °C, and 100 °C are shown in Fig. 10(a). The interference spectra are stable with increasing temperature, indicating that the sensor is insensitive to temperature changes. Multiple sets of interference spectra are obtained at different temperatures, and the fitted curve of the wavelength corresponding to the interference peak and temperature is shown in Fig. 10(b). The prediction of wavelength change with temperature at the 95 % confidence level is shown in the colored region. The temperature sensitivity of the sensor is 2.2 pm/°C, and the temperature cross-sensitivity is 0.20 με/°C, indicating that temperature variations have very little effects on the strain measurements. The silicon-air-FP is more sensitive to temperature changes than the air-FP, however, the FSR of the silicon-air-FP structure is very small, which

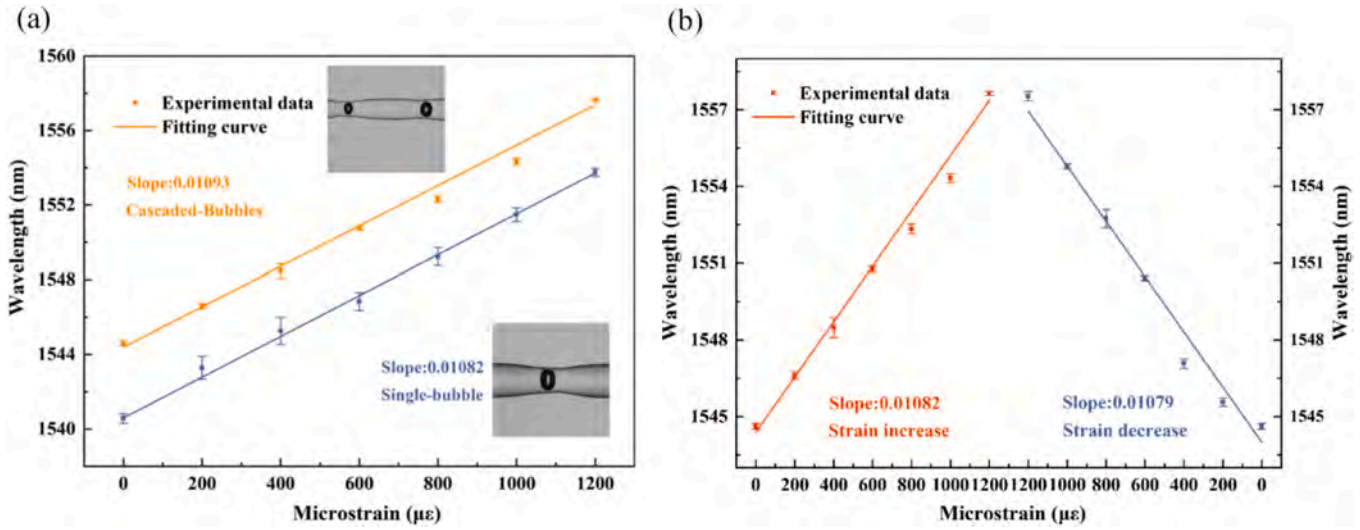

Fig. 12. Performance comparisons between (a) single-bubble structure and (b) cascaded-bubble structure (sensor S3).

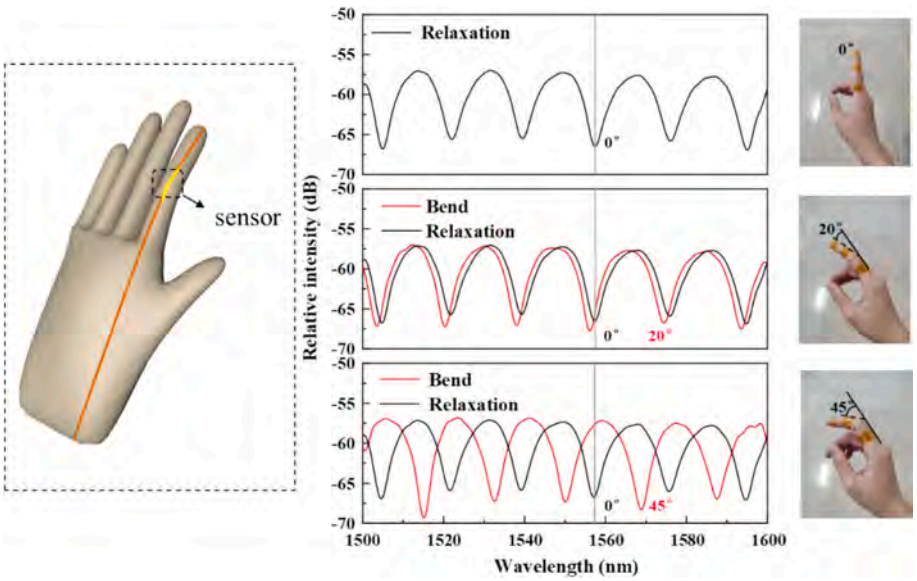

Fig. 13. Finger flexion experiment.

makes the wavelength shift of the spectrum dominated by the two FP cavities little when affected by the temperature, and thus the synthesized spectra show insensitivity to temperature changes.

Industrial infrared applications typically necessitate elevated temperature environments. The sensor was placed inside a constant-temperature heating platform, and then the temperature is raised to 200 °C. Fig. 11 (a) represents the linear fitting curves of temperature and wavelength for high temperature variations. The experimental results show that the sensor remains insensitive to temperature under high-temperature conditions, with a temperature sensitivity of 2.38 pm/°C. Furthermore, an experimental setup as shown in Fig. 11 (b) is established to evaluate the sensor's performance under practical disturbances. Repeated strain measurements were conducted within the 130–170 °C range to simulate potential temperature variations in industrial environments. It is found that while temperature fluctuations slightly degrade the sensor's sensitivity, their overall impact remains relatively minor.

A comparison of a single intact bubble without cutting and with cascading bubbles formed after cutting is shown in Fig. 12 (a). Under strain conditions ranging from 0 to 1200 με, the cascaded structure exhibits lower standard deviation in repeated measurements compared to the single-cavity design, while maintaining comparable sensitivity. The repeatability of the cascade structure sensor is verified as shown in Fig. 12(b). The slopes of the fitted curves of wavelength and strain are very similar during the process of strain increase and decrease, and the error bars are also relatively small. The result indicates that this sensor has good stability.

To assess the monitoring of human motor functions in rehabilitation, the sensor is placed on finger joints to detect the bending of the finger joints. Our experiments reveal that the interference spectrum exhibits obvious and regular changes when the joints are bent. This is because when the finger joints bend, the FP cavity is subjected to the axial strain component. The FP cavity of the sensor is affected by external forces, and then its cavity length changes, which is consistent with the previous mechanism of strain action. [30,31] clearly proved the relationship between bending and strain through rigorous formula derivation, and successfully measured the bending of the fiber FPI sensor through experiments. Although the direction in which the optical fiber is stretched is spatially complex when the finger joints bend, essentially, the optical response of the air cavity is mainly related to axial stretching/

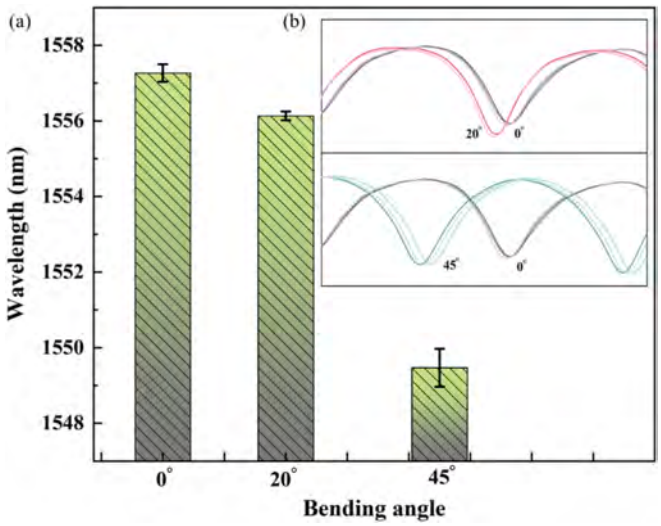

Fig. 14. (a) Error bars for the relationship between bending angle and wavelength shift; (b) Spectrum of multiple cycle bending experiment.

the presentation of the error bar range.

Table 2 compares the properties of our strain sensor with those of similar strain sensors reported recently. Compared to [5102027], the proposed sensor can be fabricated with only single-mode optical fiber and fusion splicer, which is easy to operate and cost-effective. The thin-walled tapered structure of [20] achieves higher sensitivity by improving strain transfer efficiency, but its lack of mechanical robustness may limit its reliability in practical applications such as finger motion monitoring. In contrast, the proposed sensor has the advantages of easy operation, temperature insensitivity and low cost. The preparation of the sensor can be completed by using a standardized fusion bonding technique without the need for a cone-drawing process, which avoids the susceptibility of the conical structure to bending disturbances. The proposed cascade air bubble strain sensor is more suitable for the monitoring of finger flexion motion.

4. Conclusion

A multi-interference FPI strain sensor with cascaded dual air cavities is designed, analyzed, and demonstrated experimentally. The air cavities are fabricated by arc discharge with a fiber fusion splicer, and the axial

Table 2
Comparison of the properties of our strain sensor with similar strain sensors reported in the recent literature.

Refs.	Types	Fabrication Methods	Strain Ranges	Sensitivity	Temperature Sensitivity
[5]	Composite based on two integrated parallel MZIs (bending and salinity)	Cleaving and splicing	0.085 m^{-1} – 0.19718 m^{-1}	127.15 nm/m^{-1}	37.5 pm/℃
[10]	Composite based on dual-FPIs (temperature and strain)	Cleaving and splicing	0–1000 με	1.23 pm/με (Silica cavity) 3.97 pm/με (Air cavity)	7.31 pm/℃ (25–300℃) 16.08 pm/℃ (300–800℃)
[18]	Round rectangular air cavity FPI (strain)	cleaving, Discharge	0–800 με	8 pm/με	4.79 pm/°C (20-80°C)
[20]	Asymmetric tapered air microbubble FPI (strain)	Taper, Discharge, splicing	0–1200 με	15.89 pm/με	1.09 pm/°C (25-200°C)
[27]	Asymmetrical air microbubble FPI (strain)	Taper, cleaving, splicing	0–1200 με	10.15 pm/με	2.4 pm/∘C (25-80℃)
This paper	Air bubble dual-FPIs (strain and bending)	cleaving, Discharge	0–1200 με	11.07 pm/με	2.2 pm/℃ (22-100℃)

compression, and the impact of non-axial strain or torsional force on the length of the air cavity is relatively small. Based on this, this sensor has the potential to further measure the finger bending strain and realize the perception of finger joint bending. Consequently, this sensor can be used to sense finger motions.

Fig. 13 presents the spectra of finger joints bent at 0°, 20°, and 45°. The black interference curve corresponds to the spectrum of the unbent finger, while the red interference curve represents that of the bent finger. As the bending angle increases, the position of the interference peak changes. In our experiment, the first spectrum is collected with the finger in the unbent state. When the finger bends by 20°, the interference spectrum is acquired. After the finger returns to the unbent state, another spectrum is recorded. After the spectrum stabilizes, the finger bends by 45°, and the same procedure is repeated. When the joint bends and then reverts to the unbent state, the positions of the interference peaks are basically the same. The sensor on the joint can be encapsulated with PDMS [32,33] to increase the flexibility and prolong its service life. During the experiment, three repetitive bending measurement operations were carried out for different bending angles (0°, 20°, and 45°), and the results are shown in Fig. 14. The error bars corresponding to the above three bending angles are generally within a relatively small range. However, the range of the error bar corresponding to 45° is significantly larger than those of the other angles. During the actual operation, it is difficult to precisely control the bending movements of fingers to the theoretical angles with the available experimental conditions. This leads to the observed expansion of error bar ranges at 45°, and it in turn affects strain is measured on an experimental platform. Experimental results reveal a strain sensitivity of 11.07 pm/με, thus enabling it to respond rapidly to tiny deformations. The stability and repeatability of the sensor are confirmed by observing the drift of the wavelength corresponding to the interference peak within 35 min. The process of applying and releasing strain in the forward and reverse directions is performed for verification. Considering the cross-effect of temperature, the sensor is placed on a thermostatic heating platform and heated up to 100 °C. The temperature sensitivity of the sensor is found to be 2.2 pm/°C, and the temperature cross-sensitivity is 0.20 με/°C, indicating that the sensor indeed has low temperature cross-sensitivity, thereby effectively avoiding interferences from temperature changes. The results reveal that the sensor has great potential in strain measurement such as the monitoring of finger motions.

CRediT authorship contribution statement

Yanshu Zeng: Writing – original draft, Software, Methodology, Investigation, Data curation, Conceptualization. **Xianli Li:** Visualization, Conceptualization. **Jingwei Lv:** Methodology, Investigation. **Jianxin Wang:** Software, Methodology. **Hongze Zou:** Software, Formal analysis. **Wei Liu:** Investigation. **Chao Liu:** Visualization, Supervision, Funding acquisition. **Paul K Chu:** Writing – review & editing, Visualization.

Declaration of competing interest

The authors declare that they have no known competing financial interests or personal relationships that could have appeared to influence the work reported in this paper.

Acknowledgments

This work was jointly supported by the Heilongjiang Provincial Natural Science Foundation of China [JQ2023F001], National Natural Science Foundation of China [12304480], Natural Science Foundation of Heilongjiang Province [LH2021F007], China Postdoctoral Science Foundation funded project [2020M670881], the National Natural Science Foundation of China (62305223), Natural Science Foundation of Guangdong Province (2022A1515110971), the project was supported in part by the Fundamental project Natural Science Foundation of Heilongjiang Province (LH2022F004), as well as City University of Hong Kong Donation Research Grants [DON-RMG 9229021 and 9220061].

Data availability

Data will be made available on request.

References

[1] J. Luo, H. Liu, H. Xing, et al., Large curvature bending measurable fiber-optic neurons for multi-joint bending perception, J. Lightwave Technol. 41 (17) (2023) 5780–5787.
[2] R. Jha, P. Mishra, S. Kumar, Advancements in optical fiber-based wearable sensors for smart health monitoring, Biosens. Bioelectron. 116232 (2024).
[3] C.S. Monteiro, M.S. Ferreira, S.O. Silva, et al., Fiber Fabry-Perot interferometer for curvature sensing, Photonic Sensors 6 (2016) 339–344.
[4] X.P. Pan, H.E. Yang, S.R. Liu, et al., High sensitivity fiber optic strain sensor based on CFBG-FPI and vernier effect, J. Lightwave Technol. 41 (21) (2023) 6831–6837.
[5] L. Li, Y. Zhang, B. Han, et al., Highly sensitive and regulatable optical fiber Vernier sensor based on two integrated parallel MZIs, J. Lightwave Technol. (2024).
[6] C. Liu, H. Chen, Q. Chen, et al., Sagnac interferometer-based optical fiber strain sensor with exceeding free spectral measurement range and high sensitivity, Opt. Laser Technol. 159 (2023) 108935.
[7] L. Li, H. Chen, M. Gu, et al., A high resolution and large measurement range strain sensor based on Sagnac loop and fiber Bragg grating in dual-wavelength erbium-doped fiber laser, J. Lightwave Technol. (2024).
[8] L. Li, H. Chen, R. Shi, et al., A dual-wavelength erbium-doped fiber laser for high resolution strain sensing with compound filter of a Sagnac loop and a long period fiber grating, Opt. Laser Technol. 175 (2024) 110787.
[9] T. Paixão, F. Araújo, P. Antunes, Highly sensitive fiber optic temperature and strain sensor based on an intrinsic Fabry–Perot interferometer fabricated by a femtosecond laser, Opt. Lett. 44 (19) (2019) 4833–4836.
[10] S. Lin, Y. Qu, F. Wang, et al., Simultaneous measurement of high temperature and strain based on miniature tip-packaged dual-FPIs, Measurement 225 (2024) 114027.
[11] F. Velazquez-Carreon, A. Perez-Alonzo, G.E. Sandoval-Romero, Temperature-compensated fiber Bragg grating sensor based on curvature sensing for bidirectional displacements measurement, Opt. Fiber Technol. 77 (2023) 103257.
[12] Z. Wang, W. Bao, P. Yang, et al., Highly Sensitive Strain Sensor based on the Vernier effect with High Extinction Ratio and Low-Temperature Cross-Sensitivity by Compact double FPI, IEEE Sens. J. 24 (6) (2024) 7896–7904.
[13] D.M. de Fátima, V. Rosa, A.C. Nepomuceno, et al., Wearable devices for remote physical rehabilitation using a Fabry-Perot optical fiber sensor: ankle joint kinematic, IEEE Access 8 (2020) 109866–109875.
[14] G. Shi, W. Wang, Y. Guo, et al., Flexible wearable fiber optic sensor for real-time human breath monitoring based on Fabry-Perot interferometer with agar film[J], Opt. Express 32 (19) (2024) 33208–33221.
[15] S. Zhang, A. Zhou, L. Yuan, Simultaneous temperature and bending sensor based on Fabry-Perot interferometer with Vernier effect, Opt. Fiber Technol. 66 (2021) 102657.
[16] Z. Wang, S. Jiang, P. Yang, et al., High-sensitivity and high extinction ratio fiber strain sensor with temperature insensitivity by cascaded MZI and FPI[J], Opt. Express 31 (5) (2023) 7073–7089.
[17] J. Wang, W. Liu, Q. Li, et al., A high-sensitivity strain sensor based on the core-offset fiber with a micro air bubble, Opt. Commun. 555 (2024) 130235.
[18] Q. Li, J. Wang, H. Mu, et al., A Fabry–Pérot interferometer strain sensor composed of a rounded rectangular air cavity with a thin wall for high sensitivity and interference contrast, Opt. Commun. 527 (2023) 128920.
[19] W. Zhang, H. Li, L. Zhu, et al., Dual-parameter optical fiber probe based on a three-beam fabry-perot interferometer, IEEE Sens. J. 21 (4) (2020) 4635–4643.
[20] J. Lv, W. Li, J. Wang, et al., High-sensitivity strain sensor based on an asymmetric tapered air microbubble Fabry-Pérot interferometer with an ultrathin wall, Opt. Express 32 (11) (2024) 19057–19068.
[21] B. Xu, M. Chen, K. Yang, et al., Ultra-high sensitivity strain sensor based on biconical fiber with a bulge air-bubble, Opt. Lett. 46 (8) (2021) 1983–1986.
[22] H. Wang, L. Hou, J. Li, et al., Fiber-optic axial-strain sensor based on in-cavity micro-bubble fabry-perot interferometer, Opt. Commun. 575 (2025) 131263.
[23] Z. Lu, C. Liu, C. Li, et al., Ultra-high sensitivity and temperature-insensitive optical fiber strain sensor based on dual air cavities, Materials 16 (8) (2023) 3165.
[24] T. Tian, K. Liang, Y. Ma, et al., A Fabry-Perot interferometer based on probe-embedded bubble for ultrasensitive strain measurement, Measurement 239 (2025) 115505.
[25] S. Liu, Y. Wang, C. Liao, et al., High-sensitivity strain sensor based on in-fiber improved Fabry–Perot interferometer, Opt. Lett. 39 (7) (2014) 2121–2124.
[26] S. Liu, K. Yang, Y. Wang, et al., High-sensitivity strain sensor based on in-fiber rectangular air bubble, Sci. Rep. 5 (1) (2015) 7624.
[27] L. Cai, J. Wang, M. Chen, et al., A high-sensitivity strain sensor based on an unsymmetrical air-microbubble Fabry-Pérot interferometer with an ultrathin wall[, Measurement 181 (2021) 109651.
[28] J. Wang, X. Lu, C. Mi, et al., Ultra-high sensitivity photonic crystal fiber sensor based on dispersion turning point sensitization of surface plasmonic polariton modes for low RI liquid detection, Opt. Express 32 (19) (2024) 32895–32908.
[29] H. Fu, Z. Sheng, W. Gao, et al., Ultra-high sensitivity surface plasmon resonance magnetic field sensor based on side-core inscribed capillary fiber, IEEE Sens. J. (2024).
[30] R. Oliveira, M. Cardoso, A.M. Rocha, Two-dimensional vector bending sensor based on Fabry-Pérot cavities in a multicore fiber, Opt. Express 30 (2) (2022) 2230–2246.
[31] B. Qi, B. Su, F. Zhang, et al., Temperature-insensitive two-dimensional vector bending sensor based on Fabry-Pérot interferometer incorporating a seven-core fiber, IEEE Photonics J. 14 (4) (2022) 1–9.
[32] R. Lu, X. Yue, Q. Yang, et al., Multi-node wearable optical sensor based on microfiber Bragg gratings, Opt. Express 32 (6) (2024) 8496–8505.
[33] Q.Q. Ge, T. Zhou, T.Y. Gong, et al., Highly sensitive measurement of finger joint angle based on a double-U tapered POF embedded in PDMS film, Opt. Fiber Technol. 76 (2023) 103236.